

Beyond coincidence: using all the data in HOM interferometry

Hamish Scott,¹ Dominic Branford,¹ Niclas Westerberg,^{2,1} Jonathan Leach,¹ and Erik M. Gauger¹

¹*SUPA, Institute of Photonics and Quantum Sciences,
Heriot-Watt University, Edinburgh, EH14 4AS, UK*

²*School of Physics and Astronomy, University of Glasgow, Glasgow, G12 8QQ, United Kingdom*

(Dated: December 26, 2022)

The Hong-Ou-Mandel effect provides a mechanism to determine the distinguishability of a photon pair by measuring the bunching rates of two photons interfering at a beam splitter. Of particular interest is the distinguishability in time, which can be used to probe a time delay. Photon detectors themselves give some timing information, however—while that resolution may dwarf that of an interferometric technique—typical analyses reduce the interference to a binary event, neglecting temporal information in the detector. By modelling detectors with number and temporal resolution we demonstrate a greater precision than coincidence rates or temporal data alone afford. Moreover, the additional information can allow simultaneous estimation of a time delay alongside calibration parameters, opening up the possibility of calibration-free protocols and approaching the precision of the quantum Cramér-Rao bound.

I. INTRODUCTION

When a pair of indistinguishable photons enter the two input ports of a balanced beamsplitter, they will always be detected in the same (randomly selected) output mode. This “bunching” of photons entails a reduction of coincident clicks between two detectors which monitor the output ports. A complete lack of detected coincidences indicates that an incoming pair of photons is perfectly indistinguishable in all degrees of freedom, including spatial, frequency, and polarisation properties; and most importantly to this work, the photons must also possess an exactly matched temporal profile. More generally, the coincidence rate constitutes a reliable and straightforward way of probing the difference between two pure photonic states. This is the effect the eponymous Hong, Ou, and Mandel demonstrated in their seminal work from 1987 [1].

Since then, the Hong-Ou-Mandel (HOM) effect has become a key tool in quantum optics [2–8]. Most relevantly to this paper, it is used in a variety of situations throughout quantum metrology: for parameters that cannot be easily or efficiently measured directly, it provides a way of estimating them through their impact on the indistinguishability of a photon pair. This is traditionally used as a way of measuring very small time delays [9–13], but can include other parameters such as polarisation [14]. A related, albeit slightly different quantum optical method for measuring path delays is quantum optical coherence tomography [15–17].

High precision time delay measurements have a variety of scientific and technological applications. It has been proposed that the imaging of delicate (biological) samples can benefit from exploiting quantum effects to limit photodamage [18–21]. For instance, to resolve the thickness of an unknown sample, such as e.g. a cell membrane, a delay can be induced in the path of a photon by allowing it to pass through the sample, accompanied by a second photon which does not pass through the sample. The simplest, and perhaps most obvious, way to

measure this delay would be to place detectors at the end of both photons’ paths and measure the difference in their respective arrival times, an approach similar to a direct time-of-flight measurement [22, 23]. However, the time-resolution of conventional single-photon detectors is orders of magnitude too poor to capture the precision needed for these measurements to provide the desired nanoscale resolution.

By contrast, HOM metrology has recently achieved attosecond resolution [10]. In this case, rather than measuring the delay directly, changes to the coincidence counts at two detectors placed at the outport ports of the HOM beamsplitter are recorded and analysed. Assuming an initial calibration with regards to all the other factors influencing this indistinguishability, the time delay can be isolated and estimated. Traditionally, this achieves sub-femtosecond resolution by scanning through and observing a shift of the entire HOM dip [6], but more sophisticated protocols can perform up to 100× better [10].

This attosecond resolution goes well beyond that of the single-photon detectors which may be used in such an experiment¹ limited to the nanosecond–picosecond range (centimetre-scale). Even allowing for the additional complexity of a HOM interferometer, this chasm seems hard to overcome with a direct timing approach. Nonetheless, we need not overlook entirely the time-resolving capabilities of single-photon detectors. Currently their time-resolution is only used for the purpose of establishing coincidence matching time windows. As we shall see, even when their precision falls short of that of HOM interferometry, making better use of their temporal information is advantageous in multiple ways.

¹ For instance, the conventional SPCM-AQRH detector has a temporal resolution of ≈ 350 ps [24], but some recent developments in detector time-resolution are approaching picosecond precision [25–28].

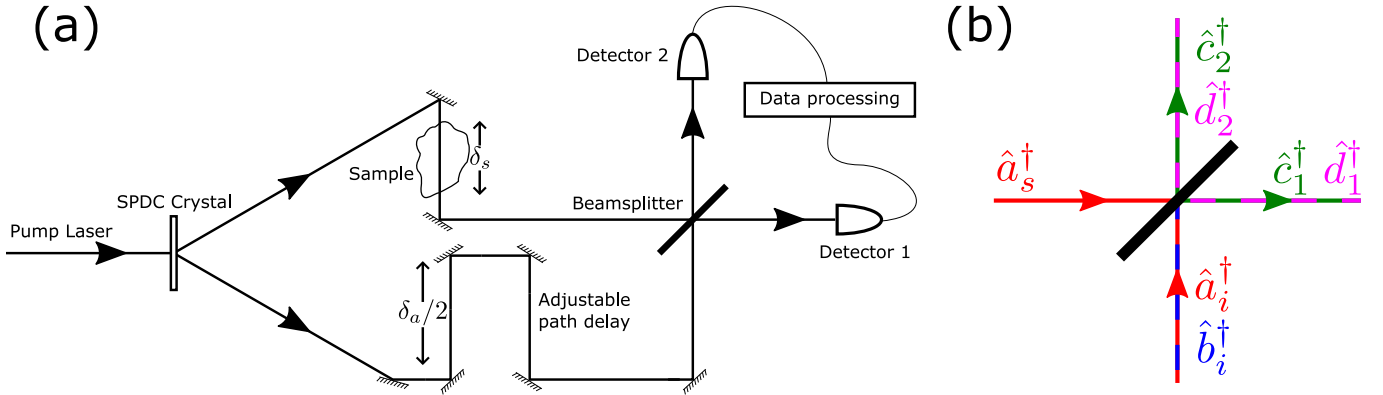


FIG. 1. (a) A schematic of our protocol. Photons are generated via spontaneous parametric down-conversion. In the top arm, the photon passes through a sample and is delayed by δ_s . An adjustable delay δ_a is placed in the lower arm. Both photons then interfere at the beamsplitter, with a relative time delay $\delta = \delta_s - \delta_a$. Detectors D1 and D2 are placed behind the beamsplitter output ports. Each detection event is then assigned to a time bin and checked for coincidence or bunching. (b) How we model the photon modes either side of the beamsplitter in Sec. III. In the lower arm, an additional orthogonal mode \hat{b}^\dagger is present to capture differences other than temporal between the photons. A mixture of modes \hat{c}^\dagger and \hat{d}^\dagger leave both beamsplitter ports.

In this Article we analyse the benefits of incorporating detector time resolution capabilities into HOM metrology. We find that not only does this upgrade the performance of HOM interferometers, but it could also facilitate a simplified protocol by eliminating the need for a separate calibration stage. Furthermore, recent developments in the feasibility of number-resolving detectors [27, 29, 30], motivate us to also analyse the benefits of photon number-resolution, and we find that these would also lead to a tangible performance enhancement. We show that by combining number and time resolving detectors the fundamental quantum Cramér-Rao bound (QCRB) can be approached with a HOM sensing protocol.

This Article is organised as follows: We start in Sec. II by explaining our HOM protocol and the model of time-resolution. Section III details the fundamental probability analysis behind our protocol, and relates it to our parameter estimation procedure in Sec. IV through the Cramér-Rao bound. In Sec. V, we derive the quantum Fisher information (QFI) for the time delay, giving the ceiling on performance for any measurement protocol, and outline one such (technically infeasible) protocol. Our main results are presented in Sec. VI, to show where our proposed protocol would sit between this ceiling and previous protocols without time- or number-resolving capabilities. Finally, we discuss our findings in Sec. VII, outlining some of the limitations of our analysis and summarising our key conclusions.

II. PROTOCOL DESCRIPTION

We consider a standard HOM protocol [31] as schematically depicted in Fig. 1, but our analysis will include detectors with time- and number-resolving capabilities. The protocol begins with a frequency-entangled pair of

photons propagate along two spatial input modes of equal path length to the HOM beamsplitter. Typically, the photon pair is generated by a pump laser in a nonlinear crystal via spontaneous parametric down-conversion (SPDC). One of the photons traverses the sample and picks up some small path length and associated time delay δ_s . The other path contains a precisely adjustable delay δ_a . Estimating δ_s could now be accomplished by scanning the adjustable delay to resolve the entire HOM dip with and without sample present and evaluating its shifts. Alternatively, we could tune δ_a such as to give minimal coincidence counts in both cases (i.e. place ourselves at the bottom of the dip) and read off the difference. Neither approach is optimal and we here follow the idea of Refs. [10, 14] to coarse-tune δ_a such that the relative delay $\delta = \delta_s - \delta_a$ maximises the information we obtain for each input photon pair. In most practical situations this point is near the inflection point of the dip and $\delta_a \gg \delta_s$. Now, comparing the difference in coincidence rate with and without sample present allows the estimation of δ_s . In the protocol employed by Refs. [10, 14], the maximum likelihood estimator for δ_s requires a fit to the previously recorded HOM dip of the setup. In those cases the employed fit was based on an inverted Gaussian and required determination of the visibility (depth of the dip) and the dip width as two calibration parameters, as well as knowledge about the photon loss rate that emerges from detector efficiency and other experimental imperfections.

We shall analyse the potential performance of HOM time delay estimation protocols for four different kinds of detectors whose behaviour is illustrated in Fig. 2. We begin with distinguishing *bucket detectors*, that are unable to discriminate the number of photons triggering a click (assuming the detector dead-time is sufficiently long such that a single detector can deliver at most one click per bunched photon pair), from *number-resolving*

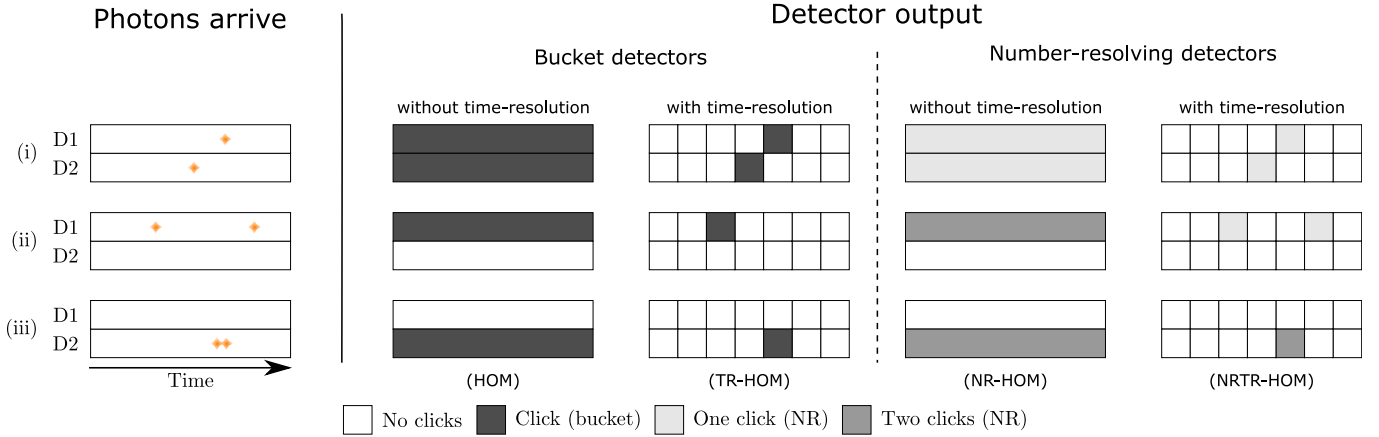


FIG. 2. Possible outputs for a pair of photons incident on the different types of detector we consider. First, standard (non-time-resolving) bucket detectors: each clicks only once whether one or more photons arrive. Then, bucket detectors with time-resolving capabilities: each detector click is now associated with a specific time bin, giving some precision as to when a photon arrives. As a consequence of detector dead time if two photons arrive at the same detector then it only clicks once, for the time bin when the earlier photon arrived. Then, number-resolving detectors without time-resolving capabilities: the detector can now differentiate between one or two photons arriving. Finally, number-resolving detectors with time-resolving capabilities: now, it can indicate when each photon arrived, up to the precision of our time bins.

detectors, which can reliably provide two clicks whenever they are hit by two bunched photons. In both cases we further consider detectors capable of providing a reliable and precise timestamp to the clicks as well as those whose signal is so smeared out that it contains little useful timing information. Previous HOM protocols have typically utilised the latter kind (or ignored available timing information for the delay estimator).

Experimental scenarios do not involve just a single photon pair and the pump laser is either in CW or pulsed operation. In the former case, the SPDC events happen randomly in time with the average duration between them determined by the pump intensity, in the latter we have a probability of generating one, or more, pairs with each pulse separated in time by the repetition frequency. In either case, HOM protocols rely on defining a coincidence time window (which is smaller than the expected time between photon pairs) to perform coincidence matching. However, as pairs can be spaced out as needed, this does not place stringent demands on the detection time-resolution capacity and is compatible with significant amounts of timing jitter (typical coincidence windows last on the order of nanoseconds). If this is the only sense in which detector timestamps are utilised, we shall refer to this scenario as detection *without time-resolution*.

By contrast, we model detection *with time-resolution* by sorting detected photons into equally-sized detection time bins of temporal width T , which reflect the timing capability and fidelity of the detection hardware. A visualisation of this time binning process, and the resultant output available, is shown in Fig. 2 for the four different types of detector we consider. Based on these outputs,

we are able to estimate the relative delay $|\delta|^2$.

III. PROBABILITY ANALYSIS

Having established the nature of the data available for the time delay estimation, we now proceed with establishing the probabilities for recording this data as a function of the time delay, loss processes and detector efficiency, and other sources distinguishability between our photon pair. We begin this calculation with the typical initial SPDC process.

A. Biphoton state

A biphoton state with fixed total energy, generated by SPDC, takes the standard form [1, 32]

$$|\psi\rangle = \int_0^{\omega_p} d\omega \phi(\omega) \hat{a}_i^\dagger(\omega) \hat{a}_s^\dagger(\omega_p - \omega) |0\rangle \quad (1)$$

with ω_p the pump frequency; and the operators $\hat{a}_i^\dagger(\omega)$ and $\hat{a}_s^\dagger(\omega_p - \omega)$ creating the two photons with frequencies ω and $\omega_p - \omega$, respectively. In the above, $\phi(\omega)$ is the joint spectral amplitude, which we take to be Gaussian and of

² As we cannot track which photon is which after the beamsplitter, sign information is lost and we can only truly estimate $|\delta|$, the size of the delay. In practice this is unimportant, but is worth remarking on as this technicality does not occur in protocols based purely on arrival time measurements, as there no beamsplitter is present.

the form

$$\phi(\omega) = (2\pi\sigma^2)^{-1/4} e^{-\frac{(\omega-\omega_p/2)^2}{4\sigma^2}}, \quad (2)$$

where σ is the spectral width [31] and $1/\sigma$ corresponds to the temporal width of our HOM dip. By assuming that our distribution of frequencies is strongly peaked around $\omega_p/2$ we can extend our ω integration over the range $(-\infty, \infty)$ to simplify our calculations.

In practice, however, the photons will not be generated in modes which are—up to the spatial mode—entirely indistinguishable. To account for this, we introduce the orthogonal mode \hat{b}_i and rewrite the operator one of our photons without loss of generality as

$$\hat{a}_i^\dagger(\omega) \rightarrow \sqrt{\alpha} \hat{a}_i^\dagger(\omega) + \sqrt{1-\alpha} \hat{b}_i^\dagger(\omega) \quad (3)$$

with the real parameter $\alpha \in [0, 1]$ describing the relative indistinguishability of our photons; α encodes the *visibility*, i.e. the ‘depth’ of the HOM dip. The state just before the beamsplitter now takes the form

$$|\psi\rangle = \int d\omega \phi(\omega) e^{-i\omega\delta_a} e^{-i(\omega_p-\omega)\delta_s} \times [\sqrt{\alpha} \hat{a}_i^\dagger(\omega) + \sqrt{1-\alpha} \hat{b}_i^\dagger(\omega)] \hat{a}_s^\dagger(\omega_p - \omega) |0\rangle. \quad (4)$$

As the photons travel towards the beamsplitter, we are interested in the relative time delay $\delta = \delta_s - \delta_a$. In which case we work with the state

$$|\psi\rangle = \int d\omega \phi(\omega) e^{i\omega\delta} \times [\sqrt{\alpha} \hat{a}_i^\dagger(\omega) + \sqrt{1-\alpha} \hat{b}_i^\dagger(\omega)] \hat{a}_s^\dagger(\omega_p - \omega) |0\rangle, \quad (5)$$

where we ignore the irrelevant global phase of $e^{-i\omega_p\delta_s}$. The HOM beamsplitter then transforms our operators as

$$\begin{aligned} \hat{a}_i^\dagger(\omega) &\rightarrow \frac{1}{\sqrt{2}} [i\hat{c}_1^\dagger(\omega) + \hat{c}_2^\dagger(\omega)], \\ \hat{b}_i^\dagger(\omega) &\rightarrow \frac{1}{\sqrt{2}} [i\hat{d}_1^\dagger(\omega) + \hat{d}_2^\dagger(\omega)], \\ \hat{a}_s^\dagger(\omega) &\rightarrow \frac{1}{\sqrt{2}} [\hat{c}_1^\dagger(\omega) + i\hat{c}_2^\dagger(\omega)], \end{aligned} \quad (6)$$

where the indices 1 and 2 denote the two output ports of our beamsplitter (or, correspondingly, which detector the photon then arrives at). Our state finally becomes

$$|\psi\rangle = \frac{1}{2} \int d\omega \phi(\omega) e^{i\omega\delta} (\sqrt{\alpha} [i\hat{c}_1^\dagger(\omega) + \hat{c}_2^\dagger(\omega)] + \sqrt{1-\alpha} [i\hat{d}_1^\dagger(\omega) + \hat{d}_2^\dagger(\omega)]) \times [\hat{c}_1^\dagger(\omega_p - \omega) + i\hat{c}_2^\dagger(\omega_p - \omega)] |0\rangle. \quad (7)$$

B. Fundamental probabilities

We proceed to determine the probabilities for photon bunching and anti-bunching (the latter corresponding to

a coincidence at the detectors). These are, respectively, cases where both photons arrive in the same detector with a delay τ , and where both photons arrive in different detectors with a delay τ .

We can represent detected coincidence events by the continuous set of positive-operator valued measures (POVMs):

$$\begin{aligned} \hat{\Pi}_c(\tau) &= \hat{c}_1^\dagger(t) \hat{c}_2^\dagger(t + \tau) |0\rangle \langle 0| \hat{c}_2(t + \tau) \hat{c}_1(t) \\ &+ \hat{c}_1^\dagger(t) \hat{d}_2^\dagger(t + \tau) |0\rangle \langle 0| \hat{d}_2(t + \tau) \hat{c}_1(t) \\ &+ \hat{d}_1^\dagger(t) \hat{c}_2^\dagger(t + \tau) |0\rangle \langle 0| \hat{c}_2(t + \tau) \hat{d}_1(t), \end{aligned} \quad (8)$$

whereas for bunching events we have the POVMs:

$$\begin{aligned} \hat{\Pi}_b(\tau) &= \hat{c}_1^\dagger(t) \hat{c}_1^\dagger(t + \tau) |0\rangle \langle 0| \hat{c}_1(t + \tau) \hat{c}_1(t) \\ &+ \hat{c}_1^\dagger(t) \hat{d}_1^\dagger(t + \tau) |0\rangle \langle 0| \hat{d}_1(t + \tau) \hat{c}_1(t) \\ &+ \hat{d}_1^\dagger(t) \hat{c}_1^\dagger(t + \tau) |0\rangle \langle 0| \hat{c}_1(t + \tau) \hat{d}_1(t). \end{aligned} \quad (9)$$

We can now evaluate the probabilities $P_c(\tau)$ and $P_b(\tau)$, namely the coincidence and bunching probabilities for a given difference in arrival times τ . Note that in this sense coincidence and bunching have lost the meaning of simultaneity and only refer to the spatial mode in which the photons are found (within the relatively long coincidence window). The fixed time t drops out in evaluating these expressions³, and after appropriate normalisation we obtain

$$P_c(\tau) = \frac{\sigma}{2\sqrt{2\pi}} e^{-2\sigma^2(\delta+\tau)^2} \left(1 + e^{8\delta\sigma^2\tau} - 2\alpha e^{4\delta\sigma^2\tau} \right), \quad (10)$$

$$P_b(\tau) = \frac{\sigma}{2\sqrt{2\pi}} e^{-2\sigma^2(\delta+\tau)^2} \left(1 + e^{8\delta\sigma^2\tau} + 2\alpha e^{4\delta\sigma^2\tau} \right). \quad (11)$$

Closer inspection shows that only at perfect visibility, $\alpha = 1$, do the photons become wholly indistinguishable at $\delta = 0$. The full derivation for these two expressions is detailed in Appendix A.

By integrating over all τ we obtain the total coincidence and bunching rates, independent of the photons’ arrival times, as usually seen in HOM analyses [31]:

$$P_{c,\text{tot}} = \int_{-\infty}^{\infty} d\tau P_c(\tau) = \frac{1}{2} \left(1 - \alpha e^{-2\sigma^2\delta^2} \right), \quad (12)$$

$$P_{b,\text{tot}} = \int_{-\infty}^{\infty} d\tau P_b(\tau) = \frac{1}{2} \left(1 + \alpha e^{-2\sigma^2\delta^2} \right). \quad (13)$$

We now introduce the binning that captures the finite time resolution of detectors into our analysis. Returning to Eqs. (10) and (11), which are valid for perfect timing, we collect all events that occur within the temporal

³ This is an artefact of using Eq. (1), we could instead use a biphoton distribution with two degrees of freedom and then integrate over all possible first arrival times t to arrive at the same answer.

width a bin T into the same indexed bin. The difference between recorded bin indices then gives coarse-grained information about the delay τ between two subsequent detection events. For bunching events we do not distinguish the photons and so any event with delay τ is identical to a delay of $-\tau$ ⁴.

Our time bins are fixed in duration and our photons are equally likely to arrive at any point within the bin. For time bin width T , and $nT < \tau < (n+1)T$, the total probability of the two photons arriving n bins apart is $[(n+1)T - \tau]/T$, and probability of them arriving $n+1$ bins apart is $(\tau - nT)/T$. We can then write the probability of a coincidence separated by n time bins, $P_{c,n}$, as

$$\begin{aligned} P_{c,0} &= 2 \left[\int_0^T d\tau \frac{T-\tau}{T} P_c(\tau) \right] \\ P_{c,n>0} &= 2 \left[\int_{(n-1)T}^{nT} d\tau \frac{\tau-(n-1)T}{T} P_c(\tau) \right. \\ &\quad \left. + \int_{nT}^{(n+1)T} d\tau \frac{(n+1)T-\tau}{T} P_c(\tau) \right], \quad (14) \end{aligned}$$

where $P_{c,0}$ is a special case as this can only happen for $\tau \leq T$. As the observed time bin difference depends only on $|\tau|$, we pick up the factor of two by restricting ourselves to positive τ . The bunching probability $P_{b,n}$ takes a similar form as

$$\begin{aligned} P_{b,0} &= 2 \left[\int_0^T d\tau \frac{T-\tau}{T} P_b(\tau) \right] \\ P_{b,n>0} &= 2 \left[\int_{(n-1)T}^{nT} d\tau \frac{\tau-(n-1)T}{T} P_b(\tau) \right. \\ &\quad \left. + \int_{nT}^{(n+1)T} d\tau \frac{(n+1)T-\tau}{T} P_b(\tau) \right]. \quad (15) \end{aligned}$$

C. Measurement probabilities

Let us now consider how these fundamental probabilities translate to actual measurement outcomes for our different detector types. At this point it is opportune to introduce the possibility of photon loss and limited detector efficiency, which can both be bundled into a single loss rate γ [10].

1. Bucket detectors

For bucket detectors, when we have a coincidence we expect both detectors to click, provided neither photon is lost. We also get a rough estimate of the time delay, up to the coarseness due to time-binning. The probability of two clicks with n time bin separation is given by $P_{2,n}^B$. If exactly one photon is lost, we will get a single click from one of the detectors, regardless of whether or not our photons bunched. In the event of bunching, we will only ever get at most one click, as a single detector is not able to discriminate between one and two arriving photons. The time bin information for a single click is irrelevant without knowing when the other photon arrived. The probability of a single click (whether from loss or bunching) is P_1^B . Neither detector will click if both photons are lost, which happens with probability P_0^B . We therefore get the following click probabilities:

$$P_{2,n}^B = (1-\gamma)^2 P_{c,n}, \quad (16)$$

$$P_1^B = 2\gamma(1-\gamma)P_{c,\text{tot}} + (1-\gamma^2)P_{b,\text{tot}}, \quad (17)$$

$$P_0^B = \gamma^2, \quad (18)$$

where as discussed the difference between time bins only applies to $P_{2,n}^B$.

2. Number-resolving detectors

For number resolving detectors, we now have four types of potential outcomes to consider. Barring photon loss, the probability of two clicks from a coincidence, $P_{2c,n}^{\text{NR}}$, remains unchanged, but we now also have a probability for two clicks when the photons bunch, $P_{2b,n}^{\text{NR}}$. The time bin information is relevant for both of these two-click outcomes and n denotes the time bin separation. If only one detector clicks, we have definitively lost exactly one photon, which occurs with probability P_1^{NR} . Finally, probability of zero clicks remain unchanged and is now denoted by P_0^{NR} . The full set of outcomes is therefore given by:

$$P_{2c,n}^{\text{NR}} = (1-\gamma)^2 P_{c,n}, \quad (19)$$

$$P_{2b,n}^{\text{NR}} = (1-\gamma)^2 P_{b,n}, \quad (20)$$

$$P_1^{\text{NR}} = 2\gamma(1-\gamma), \quad (21)$$

$$P_0^{\text{NR}} = \gamma^2. \quad (22)$$

IV. PARAMETER ESTIMATION

To address the question of how well we can extract δ , and thus δ_s , given a record of measurement data in the form described above, we turn to the theory of parameter estimation theory. The following section introduces the relevant concepts, at first in general terms and then applied to our specific scenario.

⁴ Coincidence events where the first photon arrives in the first detector rather than the second [positive and negative delays given Eq. (8)] are observably distinct, but as the first photon is equally likely to end up at either detector the distinction provides no additional information.

A. Probability distributions

The Cramér-Rao bound (CRB) can be used to bound the variance of an unbiased estimator $\tilde{\theta}$ of unknown parameter(s) θ as [33, Chap. 3]

$$\text{cov}(\tilde{\theta}) \geq \frac{1}{N} \mathbf{F}^{-1}(\theta) , \quad (23)$$

where $\mathbf{F}(\theta)$ is the Fisher information matrix (FIM) and N the number of repetitions of the experiment. For a probability distribution $P(m|\theta)$ with outcomes $m \in \mathcal{M}$ the FIM is defined with elements

$$[\mathbf{F}(\theta)]_{i,j} = \sum_{m \in \mathcal{M}} \frac{1}{P(m|\theta)} \frac{\partial}{\partial \theta_i} P(m|\theta) \frac{\partial}{\partial \theta_j} P(m|\theta) . \quad (24)$$

The maximum likelihood estimator is an estimator which is, in general, asymptotically consistent and efficient, meaning that in the limit $N \rightarrow \infty$ it is both unbiased and its variance saturates the CRB [33, Chap. 7].

Each diagonal term of the FIM $[\mathbf{F}(\theta)]_{i,i}$ corresponds to the single-parameter classical Fisher information (CFI) for the i^{th} element of θ , which we denote F_{θ_i} as shorthand. This quantifies the amount of information about θ_i that is gained from an average individual measurement. The off-diagonal terms represent covariance between the parameters, from which the correlations can be obtained. These correlations can give rise to indeterminate FIMs for which the parameters $\{\theta_i\}$ cannot all be estimated simultaneously, while a subset of the parameters may still be estimable if the remaining parameters are known (e.g. through a calibration stage).

Our HOM approach is parameterised by the set $\theta_i \in \{\delta, \alpha, \sigma, \gamma\}$. In the following we will be concerned with evaluating scalar and vector bounds for the different probability distributions (detector configurations) discussed in Sec. III. Estimating δ alone will be our primary focus, however we will also look at the potential for estimating calibration parameters independently of and in parallel with δ . For the latter (multi-parameter) setting the rank of the FIM is of particular value, identifying the number of independent parameters which can be estimated.

The traditional binary outcome HOM protocol is a simple case where we can see that—operating at a fixed point in the HOM dip—the coincidence rate can be modified by either changing α or δ . Hence, it is not possible to estimate δ without knowing α , and this gives rise to the need for a calibration stage [10]. We discuss this in more detail later and in Appendix C.

B. Quantum states

The statistics of different detectors can be considered as different POVMs acting on the same quantum state⁵. The QFI is an upperbound to the CFI for quantum systems which depends only on the quantum state and so independent of the measurement used. In the context of the CRB it gives rise to the QCRB [34–36]

$$\text{var}(\tilde{\theta}) \geq \frac{1}{NF_\theta} \geq \frac{1}{NH_\theta} , \quad (25)$$

where we give only the single-parameter bound and H_θ is the single-parameter QFI. For the purposes of parameters encoded in quantum states, it is now the QCRB that sets the ultimate limit on the precision of an estimator. The single-parameter QCRB corresponds to the precision we would obtain from an optimal measurement [34, 35]. For a pure state, the single-parameter QFI has the relatively simple form [35]:

$$H_\theta = 4[\langle \partial_\theta \psi | \partial_\theta \psi \rangle + (\langle \partial_\theta \psi | \psi \rangle)^2] . \quad (26)$$

V. BENCHMARKS

A. Quantum Fisher information

The parameter of particular interest to us is the time delay δ . In order to establish an upper bound on the observable information of δ , we now derive the QFI for δ for our biphoton state. Since the QFI is invariant under parameter-independent unitary transformations [36], we are free to return to our biphoton state in the form given in Eq. (4), after it has picked up the time delay δ but before interaction at the beamsplitter.

By writing the biphoton spectral amplitude as univariate (as is customarily done for down-converted photon pairs) we have implicitly evaluated a delta function in the bivariate biphoton spectral amplitude, which requires some additional care with regards to normalising the state. To calculate the QFI, we thus introduce the quantisation volume V and ‘renormalise’ both the Dirac delta function such that $\delta_D(0) = V$, and the joint spectral amplitude by the replacement $\phi(\omega) \rightarrow \phi(\omega)/\sqrt{V}$ [37, Chap. 4, 6] Our normalised state now takes the form

$$|\psi\rangle = \frac{1}{\sqrt{V}} \int d\omega \phi(\omega) e^{i\omega\delta} \times (\sqrt{\alpha} \hat{a}_i^\dagger(\omega) + \sqrt{1-\alpha} \hat{b}_i^\dagger(\omega)) \hat{a}_s^\dagger(\omega_p - \omega) |0\rangle . \quad (27)$$

Equation (26) can be used to calculate the QFI from Eq. (27) through

$$\langle \partial_\delta \psi | \psi \rangle = -i \int d\omega \phi(\omega)^2 \omega = -\frac{i\omega_p}{2} , \quad (28)$$

⁵ Although we applied loss and time binning to the probabilities Eqs. (10) and (11), these could equally be modelled by different POVMs.

and

$$\langle \partial_\delta \psi | \partial_\delta \psi \rangle = \int d\omega \phi(\omega)^2 \omega^2 = \sigma^2 + \frac{\omega_p^2}{4}, \quad (29)$$

full derivations for which are given in Appendix B. We can then combine Eqs. (26), (28) and (29) to obtain

$$H_\delta = 4\sigma^2. \quad (30)$$

Our expression for the QFI agrees with that obtained in Ref. [11] for frequency-entangled input photons when taking the limit of vanishing frequency detuning. We note that Eq. (30) has no dependence on α . Therefore, any optimal measurement protocol should be unaffected by the relative indistinguishability of the two photons. Additionally, there is no dependence on δ itself: the maximum information should be obtainable regardless of the specific size of the delay. These are both in contrast to our HOM protocols, where the CFI depends strongly on both α and δ , as we shall see in the following.

B. Time of flight protocol (no-HOM)

An optimal measurement scheme, which maximises the CFI is, perhaps unsurprisingly, trivially obvious: we use time-resolving detectors with infinite precision. No beamsplitter appears in this protocol, we eliminate the HOM effect entirely and simply place detectors at the ends of the paths for both photons. This has the additional benefit that we never lose track of which photon is which, and can now even distinguish between positive and negative δ .

We start by outlining this protocol and analysing its performance. Using the same pre-beamsplitter state given in Eq. (27) we take the set of POVMs

$$\hat{\Pi}^{\text{NH}}(\tau) = \hat{a}_i^\dagger(t) \hat{a}_s^\dagger(t + \tau) |0\rangle \langle 0| \hat{a}_s(t + \tau) \hat{a}_i(t) + \hat{b}_i^\dagger(t) \hat{a}_s^\dagger(t + \tau) |0\rangle \langle 0| \hat{a}_s(t + \tau) \hat{b}_i(t) \quad (31)$$

for which the probability $P^{\text{NH}}(\tau)$ that our photons arrive at the detectors with temporal separation τ is, with appropriate normalisation,

$$P^{\text{NH}}(\tau) = \sqrt{\frac{2}{\pi}} \sigma e^{-2\sigma^2(\delta-\tau)^2}. \quad (32)$$

The full derivation for this expression is detailed in Appendix A. Sampling directly from this distribution the CFI matches the QFI of $4\sigma^2$.

We now apply the binning procedure as described in Sec. III to find the probability that our photons arrive n time bins apart. Now that we can distinguish between positive and negative δ (as we know which arm each detected photon travelled along), it is important to distinguish positive and negative n . The probability that the

photon passing through the sample arrives n time bins after the other photon is therefore

$$P_n^{\text{NH}} = \int_{(n-1)T}^{nT} d\tau \frac{\tau - (n-1)T}{T} P^{\text{NH}}(\tau) + \int_{nT}^{(n+1)T} d\tau \frac{(n+1)T - \tau}{T} P^{\text{NH}}(\tau). \quad (33)$$

We insert the photon loss rate γ and obtain the measurement probabilities

$$P_{2,n}^{\text{NH}} = (1 - \gamma)^2 P_n^{\text{NH}}, \quad (34)$$

$$P_1^{\text{NH}} = 2\gamma(1 - \gamma), \quad (35)$$

$$P_0^{\text{NH}} = \gamma^2, \quad (36)$$

for two clicks (with n bin separation), one click, or zero clicks, respectively.

We will refer to this protocol as ‘no-HOM’ and use it as a benchmark of the raw time resolution of the detectors alone. We shall see that whilst it performs much worse than HOM protocols at low and moderate detector time resolution, it can beat the HOM approach at a sufficiently high resolution. Note that this is similar to the time-of-flight protocols of Ref. [22, 23, 28], where direct timing information is used to construct an image. The typical resolutions involved in such a set-up are 10–30 ps, although Ref. [28] reports a temporal resolution of $\simeq 2.6$ ps. Taking the limit of infinite temporal resolution for the no-HOM approach yields the optimal protocol, and with $\gamma = 0$ we find $F_\delta \rightarrow H_\delta$ as $T \rightarrow 0$ for all δ and α .

C. Loss-adjusted quantum Fisher information

For $\gamma \neq 0$ we note that information can only be obtained when neither photon is lost, which happens with probability $(1 - \gamma)^2$. Allowing only for measurements to happen when both photons are detected, the effective QFI will be reduced by the probability of neither photon being lost

$$H_\delta^{\text{2ph}}(\gamma) = (1 - \gamma)^2 H_\delta = 4\sigma^2(1 - \gamma)^2. \quad (37)$$

This ‘two-photon conditioned QFI’ is distinct from the actual QFI of the loss-affected mixed state: the QFI for the mixed state subjected to loss will be larger, as when a single photon is lost, the state of the other photon still possesses some parameter-dependence. However, that larger information is not readily accessible without additional information—such as the time at which the photons were initially generated—or resources in the measurement⁶. As we are principally interested in the relative delay between the two photon arrival times rather

⁶ Similar subtleties are observed in phase estimation where additional resources or knowledge can be required to realise QFIs [38, 39].

than the absolute length of either path we favour using $H_\delta^{2\text{ph}}$ as a loss-adjusted point of comparison.

VI. RESULTS

In the following, it will be convenient to express our temporal parameters δ and T in units of $1/\sigma$, i.e. in units of the inverse of the photons' spectral width which is equal to the width of the HOM dip. This yields the CFI F_δ in units of σ^2 , though note that we will usually rescale this as a fraction of $H_\delta^{2\text{ph}}$, the two-photon conditioned QFI. We refer to this rescaled quantity, $F_\delta/H_\delta^{2\text{ph}}$, as the relative information I_{rel} .

Only for detectors without time-resolution are we able to obtain relatively neat closed-form expressions for the CFI. We obtain the single parameter CFIs for δ (as well as multi-parameter CFI matrices) in Appendix C. The time-delay CFIs are given by Eqns. (C5) and (C6). For the cases with time-resolution, the CFIs are unfortunately less amenable for analytical inspection, but can be straightforwardly evaluated numerically.

We compare four different configurations of the HOM

protocol: First, the standard HOM protocol (such as that in Ref. [10]) involving bucket detectors and no time-resolution; this will be referred to as the HOM protocol without qualifiers. We assign the label NR-HOM to a protocol that is enhanced with number-resolving detectors. Further, we consider two variants without and with time-resolution, referred to as TR-HOM and NRTR-HOM, respectively. The no-HOM protocol outlined in Sec. V will serve as a benchmark throughout.

A. Optimal delay

In Fig. 3 we compare I_{rel} for our different protocols as a function of δ . All HOM protocols with visibility $\alpha < 1$ feature two characteristic peaks that are symmetric about $\delta = 0$ with peak positions that differ slightly between the different protocols. Adjusting δ_a allows us to tune δ such that it falls into a favourable local environment near the maximal CFI, enabling operation close the optimal point. The no-HOM protocol is also shown and indicates the background information coming purely from the time bin information of our measurements (for the case of detectors with time resolution).

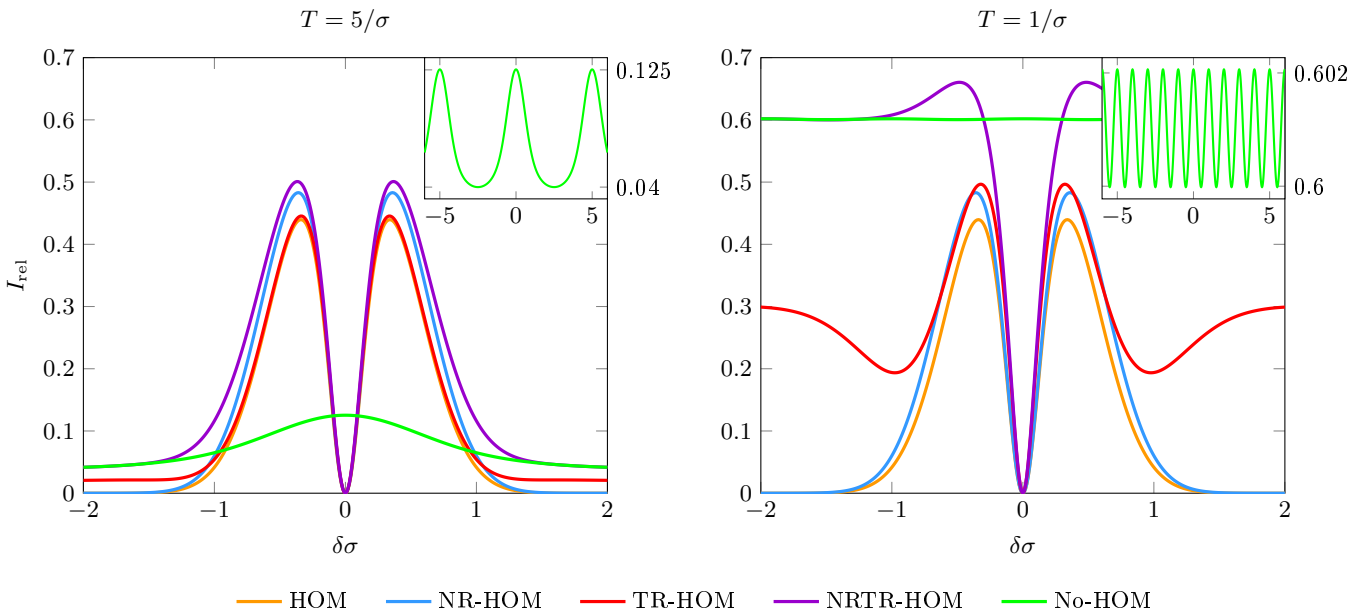


FIG. 3. Comparison of the relative information $I_{\text{rel}} = F_\delta/H_\delta^{2\text{ph}}$, the classical Fisher information as a fraction of the two-photon conditioned quantum Fisher information, for our protocol configurations as we vary the delay δ . We contrast the basic HOM protocol with bucket detectors against versions with number-resolving (NR-HOM) and time-resolving (TR-HOM) detectors, as well both enhancements simultaneously (NRTR-HOM). Finally, no-HOM is a time of flight protocol that solely measures arrival times. We set $\alpha = 0.9$ and $\gamma = 0.4$, and the time bin widths $T = 5/\sigma$ on the left, and $T = 1/\sigma$ on the right. All HOM protocols feature peaks in the information equally spaced around $\delta = 0$. The no-HOM protocol displays (non-sinusoidal) oscillation in the relative information with period equal to T . The amplitude of this oscillation reduces with low T , and can be seen in more detail in the insets. The right plot shows the benefits of reduced T (better resolution) by the increased information.

There is a slight (non-sinusoidal) oscillation in the no-HOM information, with period equal to the time bin width. This emerges as it is optimal to have $\delta = nT$, for some integer n . This reduces the variance in the measured bin difference, and the most likely result will be a difference of n bins. By comparison, for $\delta = (n + \frac{1}{2})T$, we will now see results primarily split between n and $n + 1$ bins, leading to a reduction in information obtained; this effect is substantial for $T = 5/\sigma$. As T shrinks, however, the no-HOM background information increases and the amplitude of these oscillations rapidly shrinks, becoming mostly negligible for $T \lesssim 1/\sigma$.

At large delay, F_δ for NRTR-HOM tends towards the no-HOM information, as we no longer get useful information from coincidence and bunching rates as the temporal modes become orthogonal. For TR-HOM, however, it instead tends towards half the no-HOM information, as half the time our photons will bunch and we can only detect the arrival of one of those photons, a measurement which carries no useful delay information.

B. Time-resolution

As we increase temporal resolution, time-resolving protocols gain an increasing advantage over their less advanced counterparts. In Fig. 3, no-HOM performs worse

than all HOM protocol configurations with $T = 5/\sigma$. However, with $T = 1/\sigma$ no-HOM only performs narrowly worse than NRTR-HOM but now beats our other HOM protocols. We can see more clearly in Fig. 4 how the maximal information varies with time resolution. Given NRTR-HOM contains the same timing information of no-HOM with additional information coming from the bunching rate, it will never perform worse. However, as $T \rightarrow 0$, timing information dominates and HOM information becomes irrelevant. Thus the two protocols achieve parity in maximal information, and both tend towards the QFI.

Without NR capabilities there is a transition between TR bucket detectors being best placed in the HOM (TR-HOM) or no-HOM configurations. In Fig. 4 this is around $T \sim 1/\sigma$, at higher time-resolutions than which the no-HOM configuration is preferable. TR-HOM falls short in this regime, as time bin information cannot be obtained from bunching events. This transition is affected by the visibility α (which limits the effectiveness of the HOM but not no-HOM protocols) with increased α allowing TR-HOM to perform competitively at higher time-resolutions.

It is worth recalling that conventional photon detectors have time-resolving abilities far worse than $1/\sigma$ of typical SPDC photons: whilst time-resolution was not used in Ref. [10], the estimated detector timing jitter on

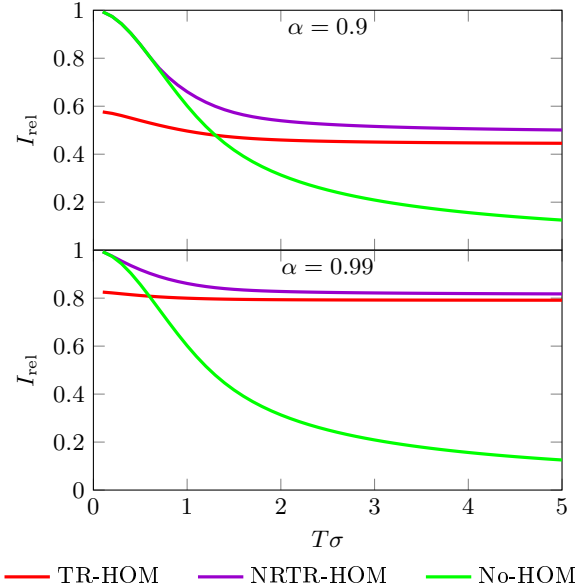


FIG. 4. The relative information I_{rel} for time-resolving protocols as we vary time bin size T . We set $\gamma = 0.4$, and δ is chosen to maximise the information; with $\alpha = 0.9$ (as in Fig. 3) in the top panel and $\alpha = 0.99$ in the bottom panel. The no-HOM protocol performs poorly at low time-resolution, but around $T = 1/\sigma$ overtakes TR-HOM and achieves parity with NRTR-HOM. As $T \rightarrow 0$, no-HOM and NRTR-HOM approach the QFI limit. Increased visibility extends the range across which a HOM-based protocol is advantageous.

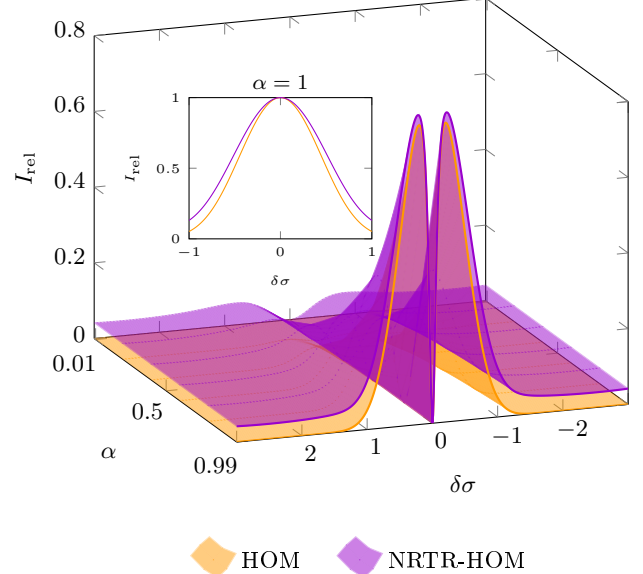


FIG. 5. The relative information I_{rel} as we vary δ and α for the two extreme HOM protocols: standard HOM (lower surface) vs NRTR-HOM (upper surface). The two characteristic peaks grow and move inwards at higher visibility; merging to a single peak at the origin that saturates the two-photon conditioned QFI for perfect visibility $\alpha = 1$ as shown in the inset. At large δ , background time bin information manifests itself in the NRTR-HOM surface not falling to zero. Other parameters are $\gamma = 0.4$ and $T = 5/\sigma$.

the order of nanoseconds results in $T\sigma > \mathcal{O}(10^2)$. Consequently, there would have been only negligible timing background information in those experiments, and HOM effect information overwhelmingly dominated.

C. Visibility & photon loss

In the following we focus on the two most extreme variants among our HOM protocols: the ‘all bells and whistles’ case of NRTR-HOM contrasted against the conventional HOM scenario. In Fig. 5 we can see how the information for our NRTR-HOM protocol varies with both δ and α . The two peaks rise rapidly as visibility is increased, moving inwards and converging to a single peak at the origin at the limit $\alpha = 1$, achieving the QFI limit at this point. At large delays information tends to the lower background level, that is obtained solely from arrival times and is thus independent of α . Our standard HOM protocol follows a similar shape though performs slightly worse. At large delays its information falls to zero, without the background information coming from simple arrival time data.

The central plot of Fig. 6 shows how the relative information I_{rel} varies with γ . For NRTR-HOM, the CFI scales linearly with $(1 - \gamma)^2$, the same dependence as in the QFI. Thus I_{rel} is constant with γ . Standard HOM performs even worse at increased photon loss rates as compared to the two-photon conditioned QFI, due to one-click measurements not only dominating over two-clicks events but also becoming less likely to indicate bunching. This reduces the available information that can be gleaned and renders most of the measurement outcomes useless.

D. Approaching the QFI

In the left plot of Fig. 6, we see that by letting the time bin width tend to 0 we can, with NRTR-HOM, approach the limit of the two-photon conditioned QFI. This then achieves the full QFI of $4\sigma^2$ with the additional realisation of $\gamma = 0$. The right plot of Fig. 6 shows that we achieve this for all sufficiently large δ , though interestingly a dip in I_{rel} remains around $\delta = 0$. As previously discussed, this is not much of a constraint, however, given the ability to adjust δ_a .

E. Multi-parameter estimation

As discussed in Sec. IV, we may want to estimate multiple parameters as a means of eliminating the need for a separate calibration stage. The most critical and tricky calibration parameter is α —loss and spectral width are easier to determine, and at least the latter is less variable. For this reason we begin with the case of wishing to estimate δ and α simultaneously.

Delay and visibility become increasingly independent at higher time-resolution, as we are better able to estimate δ independent of any coincidence/bunching information. By constructing the FIM for these two parameters, we see in Fig. 7 how this effect manifests as the determinant increases as time bin width shrinks. This is analogous to an increase in the single-parameter CFI, indicating increased information and thus making estimation more efficient. For a fixed time bin width, if we instead vary δ we see a similar shape to that in Fig. 3.

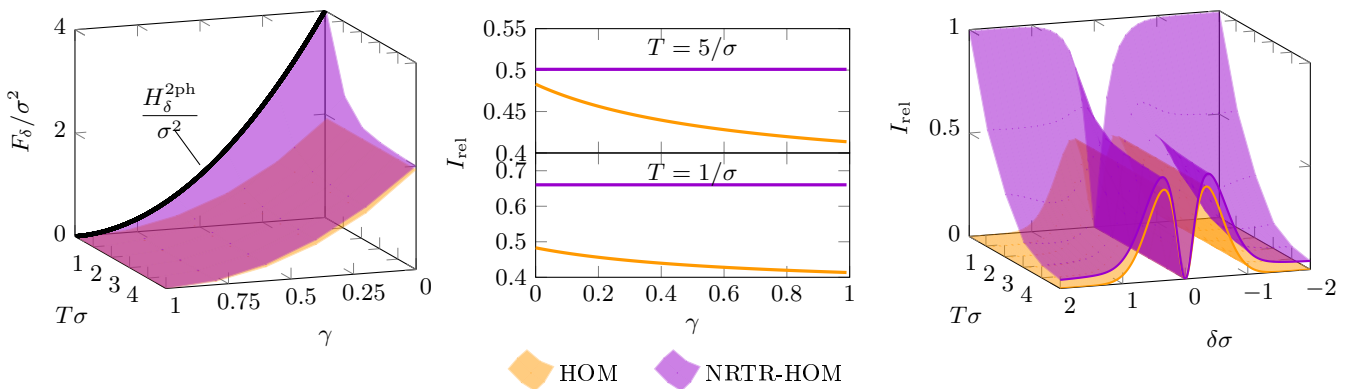


FIG. 6. Left: F_δ as a function of γ and T . The standard HOM case is independent of T and thus only depends on γ . Here, $\alpha = 0.9$ and δ is chosen to maximise information at each point. Both protocols naturally perform better at lower γ , and NRTR-HOM approaches $H_\delta^{2\text{ph}}$ as $T \rightarrow 0$. Centre: $F_\delta/H_\delta^{2\text{ph}}$ as a function of γ . δ is chosen to maximise information at each point. For NRTR-HOM, the relative information remains constant as γ is varied, but for standard HOM the information decreases at higher γ (see text). $T = 5/\sigma$ for the top plot, $T = 1/\sigma$ for the bottom plot, $\alpha = 0.9$ is used in both. Right: the relative information I_{rel} , taking $\gamma = 0.4$, and varying δ and T . At vanishingly small T , NRTR-HOM achieves the QFI limit for sufficiently large δ .

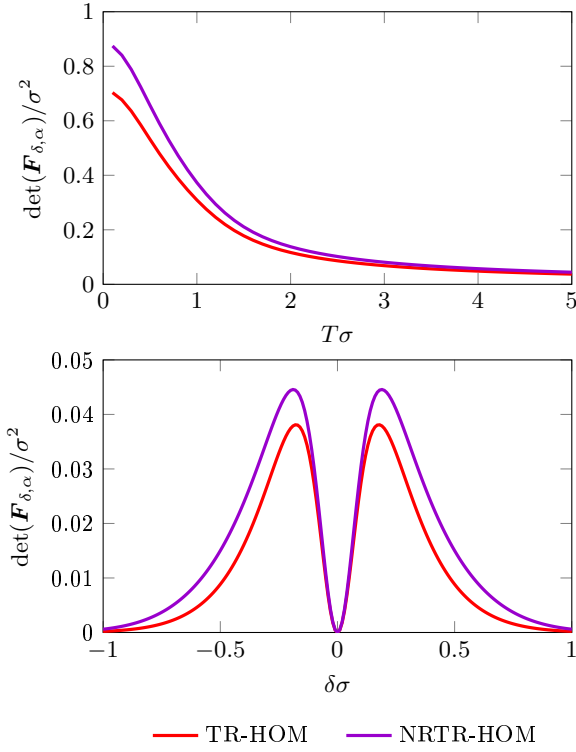


FIG. 7. The determinant of the Fisher information matrix for parameters δ and α for $\alpha = 0.9$ and $\gamma = 0.4$. Top: for fixed $\delta = 0.2/\sigma$ and varying time bin size T . At higher time-resolution (smaller T) the determinant increases, and the benefit of number-resolving detectors become more pronounced. Bottom: for fixed $T = 5/\sigma$ and varying δ . The two peaks in the determinant represent the optimal points for estimating δ and α simultaneously.

The optimal points for estimating δ and α simultaneously are given by the peaks in the determinant. The requirement that we now estimate α alongside δ causes the peaks to shift inwards as compared to those in Fig. 3, as α itself is best estimated close to the origin (see Appendix D for further discussion).

Further investigating the eigenvalues can give a clearer idea of what the independently estimable parameters may be and their attainable precision [40, 41], and even reveal ‘sloppiness’: how many effective parameters are required to capture a model’s behaviour [42]. Our focus has been on estimating δ and so it may be beneficial to cast the other parameters as nuisance parameters [43, 44], however there are cases where tracking a parameter such as visibility is of independent interest [45, 46].

VII. DISCUSSION AND CONCLUSION

Our analysis shows how Hong-Ou-Mandel metrology can be boosted by the introduction of more sophisticated detector hardware. In particular, a switch from bucket detectors (i.e. detectors that are incapable of resolving more than one photon simultaneously or with a short

time gap due to dead time) to number-resolving detectors yields significant improvements regardless of the detector time-resolving capabilities, an immediate boost in Fisher information of 9.9 % at our benchmark of $\alpha = 0.9$, $\gamma = 0.4$. This increase relative to bucket performance is even further pronounced at lower visibility and higher photon loss. Number-resolving detectors have historically suffered additional drawbacks, such as extremely low operating temperatures making them costly to implement [47, 48], however, recent developments [27, 29, 30] suggest such detectors may soon become more viable.

Unlocking the increase in accessible information offered by time-resolving detectors may present a more significant challenge. Taking Lyons *et al.* [10] as an example: here the 808 nm downconverted photons, together with a 10 nm bandpass filter, lead to a dip of spatial width $\approx 65 \mu\text{m}$. This corresponds to a temporal width of $\approx 0.2 \text{ ps}$ and spectral width $\sigma \approx 4.6 \text{ ps}^{-1}$. To see a noticeable increase in precision would require detector resolution approaching the order of 1 ps, leading to an improvement of around 1.3 %, or 14 % if the detectors are also number-resolving. This is as-of-yet beyond the precision offered by conventional modern detectors though some recent work is nearing this level of precision. Work by Zadeh *et al.* [26], Korzh *et al.* [28] show superconducting nanowire detectors offering sub-10 ps resolution while retaining high detector efficiency. Whilst the precision increase from these particular detectors would still be modest, this nonetheless already opens up the possibility of a multi-parameter estimation scheme in order to eliminate the need for determining the width, loss, and most importantly visibility calibration parameters separately.

It would take a detector time resolution as high as 0.2 ps (or, more generally, on the order of the HOM dip width) for no-HOM approach, to acquire competitive performance: no-HOM would then perform 36 % better than HOM, and also beat TR-HOM, but still fall short of NRTR-HOM which boast a 50 % increase over HOM. If resolution were further doubled, no-HOM would perform nearly on par with time- and number-resolving HOM which features an increase of 95 % over basic HOM. Therefore, detectors with such high time resolution would obviate the need for a HOM protocol altogether: in this case almost all information can be obtained by directly measuring arrival times, and extra information gained from coincidence/bunching results becomes negligible, and this would moot the advantage of number-resolving detectors, which are unnecessary in a no-HOM setup. However, this level of temporal resolution (combined with the desirable high efficiency and low dark counts) is unlikely to become available in the near future, if ever, so HOM interferometry will likely remain the uncontested approach towards estimating phase-non-sensitive group velocity delays.

At this point, it is worth discussing a few simplifying assumptions which we have made in our analysis: first, we have assumed exactly one input photon pair per co-

incidence matching time window. In reality, SPDC does not generate photons at a constant rate and could, at least in CW mode, generate two pairs in rapid succession, or none at all for a given window, with the latter case not affecting our benchmarking conclusions, but bearing on the rate at which information is accumulated. Next, for our bucket detectors we have assumed that these have a dead time exceeding any possible delay between the two photons, i.e. such a detector could only ever register at most one photon from a given pair. Finally, we have omitted any consideration of detector dark counts: instances where a detector randomly clicks without a photon arrival. The prevalence of dark counts imposes limits on the rate at which we want to generate photons: too low a rate and dark counts will dominate, too high and we risk falling foul of dead times or associating photons from different pairs within the same coincidence window. These are all key things to consider in any experimental setup, but should have negligible impact on our benchmarking efforts to compare performance, provided an appropriate rate of photon generation is chosen.

In summary, while HOM metrology has often been presented as a means to circumvent limitations in detector resolution, we are now in fact nearing the point where state-of-the-art detectors will possess sufficient resolution

to augment the conventional HOM protocol for resolving path length delays. These gains will be gradual, as resolution improves. Whilst engineering a narrower or more structured HOM dip can boost the performance of HOM protocols, further extending their lead over direct time-of-flight measurements, in situations where a sufficiently narrow dip is not possible, the need for HOM approach may be eliminated in the longer-term should the native detector resolution surpass the order of the dip width. Likewise, we have shown that HOM protocols can be significantly enhanced through the adoption of number-resolving detectors allowing HOM-based protocols to remain superior even as timing resolution is improved. Perhaps most importantly in the near future, our analysis highlights the possibility of simplified calibration-free HOM metrology and points the way toward asymptotically approaching the precision of the QCRB.

ACKNOWLEDGMENTS

The authors thank George Knee for discussions and feedback. This work was supported by UK EPSRC Grant EP/R030413/1. NW also wishes to acknowledge financial support from UK EPSRC Grant EP/R513222/1.

[1] C. K. Hong, Z. Y. Ou, and L. Mandel, Measurement of subpicosecond time intervals between two photons by interference, *Phys. Rev. Lett.* **59**, 2044 (1987).

[2] A. N. Boto, P. Kok, D. S. Abrams, S. L. Braunstein, C. P. Williams, and J. P. Dowling, Quantum interferometric optical lithography: Exploiting entanglement to beat the diffraction limit, *Phys. Rev. Lett.* **85**, 2733 (2000).

[3] P. Kok, W. J. Munro, K. Nemoto, T. C. Ralph, J. P. Dowling, and G. J. Milburn, Linear optical quantum computing with photonic qubits, *Rev. Mod. Phys.* **79**, 135 (2007).

[4] X.-s. Ma, S. Zotter, J. Kofler, R. Ursin, T. Jennewein, C. Brukner, and A. Zeilinger, Experimental delayed-choice entanglement swapping, *Nature Physics* **8**, 479 (2012).

[5] D. Ferraro, J. Rech, T. Jonckheere, and T. Martin, Non-local interference and hong-ou-mandel collisions of single bogoliubov quasiparticles, *Phys. Rev. B* **91**, 075406 (2015).

[6] D. Giovannini, J. Romero, V. Poto ek, G. Ferenczi, F. Speirits, S. M. Barnett, D. Faccio, and M. J. Padgett, Spatially structured photons that travel in free space slower than the speed of light, *Science* **347**, 857–860 (2015).

[7] J.-H. Kim, T. Cai, C. J. K. Richardson, R. P. Leavitt, and E. Waks, Two-photon interference from a bright single-photon source at telecom wavelengths, *Optica* **3**, 577 (2016).

[8] C. Agnesi, B. D. Lio, D. Cozzolino, L. Cardi, B. B. Bakir, K. Hassan, A. D. Frera, A. Ruggeri, A. Giudice, G. Vallone, P. Villoresi, A. Tosi, K. Rottwitt, Y. Ding, and D. Bacco, Hong–Ou–Mandel interference between independent III–V on silicon waveguide integrated lasers, *Opt. Lett.* **44**, 271 (2019).

[9] C. Olindo, M. A. Sagioro, C. H. Monken, S. Pádua, and A. Delgado, Hong-ou-mandel interferometer with cavities: Theory, *Phys. Rev. A* **73**, 043806 (2006).

[10] A. Lyons, G. C. Knee, E. Bolduc, T. Roger, J. Leach, E. M. Gauger, and D. Faccio, Attosecond-resolution hong-ou-mandel interferometry, *Science Advances* **4**, eaap9416 (2018).

[11] Y. Chen, M. Fink, F. Steinlechner, J. P. Torres, and R. Ursin, Hong-ou-mandel interferometry on a biphoton beat note, *npj Quantum Information* **5**, 43 (2019).

[12] Y. Yang, L. Xu, and V. Giovannetti, Two-parameter hong-ou-mandel dip, *Scientific Reports* **9**, 10821 (2019).

[13] S. Restuccia, M. Toroš, G. M. Gibson, H. Ulbricht, D. Faccio, and M. J. Padgett, Photon bunching in a rotating reference frame, *Physical Review Letters* **123**, 110401 (2019).

[14] N. Harnchaiwat, F. Zhu, N. Westerberg, E. Gauger, and J. Leach, Tracking the polarisation state of light via hong-ou-mandel interferometry, *Opt. Express* **28**, 2210 (2020).

[15] M. B. Nasr, B. E. A. Saleh, A. V. Sergienko, and M. C. Teich, Demonstration of dispersion-canceled quantum-optical coherence tomography, *Phys. Rev. Lett.* **91**, 083601 (2003).

[16] M. D. Mazurek, K. M. Schreiter, R. Prevedel, R. Kaltenbaek, and K. J. Resch, Dispersion-cancelled biological imaging with quantum-inspired interferometry, *Scientific Reports* **3**, 1582 (2013).

[17] M. Taylor, *Quantum Microscopy of Biological Systems* (Springer International Publishing, 2015).

[18] F. Wolfgramm, C. Vitelli, F. A. Beduini, N. Godbout,

and M. W. Mitchell, Entanglement-enhanced probing of a delicate material system, *Nature Photonics* **7**, 28 (2013).

[19] M. A. Taylor and W. P. Bowen, Quantum metrology and its application in biology, *Physics Reports* **615**, 1–59 (2016).

[20] C. A. Casacio, L. S. Madsen, A. Terrasson, M. Waleed, K. Barnscheidt, B. Hage, M. A. Taylor, and W. P. Bowen, Quantum correlations overcome the photodamage limits of light microscopy (2020), [arXiv:2004.00178 \[physics.optics\]](https://arxiv.org/abs/2004.00178).

[21] G. T. Garces, H. M. Chrzanowski, S. Daryanoosh, V. Thiel, A. L. Marchant, R. B. Patel, P. C. Humphreys, A. Datta, and I. A. Walmsley, Quantum-enhanced stimulated emission microscopy (2020), [arXiv:2004.10733 \[quant-ph\]](https://arxiv.org/abs/2004.10733).

[22] S. Pellegrini, G. S. Buller, J. M. Smith, A. M. Wallace, and S. Cova, Laser-based distance measurement using picosecond resolution time-correlated single-photon counting, *Measurement Science and Technology* **11**, 712 (2000).

[23] R. Tobin, A. Halimi, A. McCarthy, X. Ren, K. J. McEwan, S. McLaughlin, and G. S. Buller, Long-range depth profiling of camouflaged targets using single-photon detection, *Optical Engineering* **57**, 1 (2017).

[24] *SPCM-AQRH Single-Photon Counting Module*, Excelitas Technologies (2020), rev 2020-04.

[25] P. Rath, A. Vetter, V. Kovalyuk, S. Ferrari, O. Kahl, C. Nebel, G. N. Goltsman, A. Korneev, and W. H. P. Perneke, Travelling-wave single-photon detectors integrated with diamond photonic circuits: operation at visible and telecom wavelengths with a timing jitter down to 23 ps, in *Integrated Optics: Devices, Materials, and Technologies XX* (SPIE, 2016).

[26] I. E. Zadeh, J. W. N. Los, R. B. M. Gourgues, G. Bulgari, S. M. Dobrovolskiy, V. Zwiller, and S. N. Dorenbos, A single-photon detector with high efficiency and sub-10ps time resolution (2018), [arXiv:1801.06574 \[physics.ins-det\]](https://arxiv.org/abs/1801.06574).

[27] D. Zhu, M. Colangelo, C. Chen, B. A. Korzh, F. N. C. Wong, M. D. Shaw, and K. K. Berggren, Resolving photon numbers using a superconducting nanowire with impedance-matching taper, *Nano Letters* **20**, 3858 (2020).

[28] B. Korzh, Q.-Y. Zhao, J. P. Allmaras, S. Frasca, T. M. Autry, E. A. Bersin, A. D. Beyer, R. M. Briggs, B. Bumble, M. Colangelo, G. M. Crouch, A. E. Dane, T. Gerrits, A. E. Lita, F. Marsili, G. Moody, C. Peña, E. Ramirez, J. D. Rezac, N. Sinclair, M. J. Stevens, A. E. Velasco, V. B. Verma, E. E. Wollman, S. Xie, D. Zhu, P. D. Hale, M. Spiropulu, K. L. Silverman, R. P. Mirin, S. W. Nam, A. G. Kozorezov, M. D. Shaw, and K. K. Berggren, Demonstration of sub-3 ps temporal resolution with a superconducting nanowire single-photon detector, *Nature Photonics* **14**, 250 (2020).

[29] B. E. Kardynal, Z. L. Yuan, and A. J. Shields, An avalanche-photodiode-based photon-number-resolving detector, *Nature Photonics* **2**, 425 (2008).

[30] S. M. Young, M. Sarovar, and F. Léonard, Design of High-Performance Photon-Number-Resolving Photodetectors Based on Coherently Interacting Nanoscale Elements, *ACS Photonics* **7**, 821 (2020).

[31] A. M. BraÅDczyk, Hong-ou-mandel interference (2017), [arXiv:1711.00080 \[quant-ph\]](https://arxiv.org/abs/1711.00080).

[32] W. P. Grice and I. A. Walmsley, Spectral information and distinguishability in type-II down-conversion with a broadband pump, *Physical Review A* **56**, 1627 (1997).

[33] S. Kay, *Fundamentals of statistical signal processing* (Prentice-Hall PTR, Englewood Cliffs, N.J, 1993).

[34] S. L. Braunstein and C. M. Caves, Statistical distance and the geometry of quantum states, *Phys. Rev. Lett.* **72**, 3439 (1994).

[35] M. G. A. Paris, Quantum estimation for quantum technology, *International Journal of Quantum Information* **07**, 125 (2009).

[36] G. Tóth and I. Apellaniz, Quantum metrology from a quantum information science perspective, *Journal of Physics A: Mathematical and Theoretical* **47**, 424006 (2014).

[37] R. Loudon, *The Quantum Theory of Light*, 3rd ed. (Oxford University Press, 2000).

[38] A. Monras, Optimal phase measurements with pure Gaussian states, *Physical Review A* **73**, 033821 (2006).

[39] M. Jarzyna and R. Demkowicz-Dobrzański, Quantum interferometry with and without an external phase reference, *Physical Review A* **85**, 011801(R) (2012).

[40] S. Ragy, M. Jarzyna, and R. Demkowicz-Dobrzański, Compatibility in multiparameter quantum metrology, *Physical Review A* **94**, 052108 (2016).

[41] E. Bisketzi, D. Branford, and A. Datta, Quantum limits of localisation microscopy, *New Journal of Physics* **21**, 123032 (2019).

[42] S. Davidson, F. A. Pollock, and E. M. Gauger, Understanding what matters for efficient exciton transport using Information Geometry, [arXiv:2004.14814v1 \[quant-ph\]](https://arxiv.org/abs/2004.14814v1) (2020).

[43] E. L. Lehmann and G. Casella, *Theory of Point Estimation*, Springer Texts in Statistics (Springer-Verlag, New York, 1998).

[44] J. Suzuki, Y. Yang, and M. Hayashi, Quantum state estimation with nuisance parameters, [arXiv:1911.02790v2 \[quant-ph\]](https://arxiv.org/abs/1911.02790v2) (2019).

[45] V. Cimini, I. Gianani, L. Ruggiero, T. Gasperi, M. Sbroscia, E. Roccia, D. Tofani, F. Bruni, M. A. Ricci, and M. Barbieri, Quantum sensing for dynamical tracking of chemical processes, *Physical Review A* **99**, 053817 (2019).

[46] V. Cimini, M. Mellini, G. Rampioni, M. Sbroscia, L. Leoni, M. Barbieri, M. Barbieri, and I. Gianani, Adaptive tracking of enzymatic reactions with quantum light, *Optics Express* **27**, 35245 (2019).

[47] F. Marsili, D. Bitauld, A. Gaggero, S. Jahanmirinejad, R. Leoni, F. Mattioli, and A. Fiore, Physics and application of photon number resolving detectors based on superconducting parallel nanowires, *New Journal of Physics* **11**, 045022 (2009).

[48] M. D. Eisaman, J. Fan, A. Migdall, and S. V. Polyakov, Invited review article: Single-photon sources and detectors, *Review of Scientific Instruments* **82**, 071101 (2011).

Appendix A: Arrival rates

1. HOM coincidence probability

In order to fully derive the fundamental coincidence rate we must evaluate $P_c(\tau) = \langle \psi | \hat{\Pi}_c(\tau) | \psi \rangle$, with $|\psi\rangle$ as given in Eq. (7) and $\hat{\Pi}_c(\tau)$ the POVMs given in Eq. (8). We also note the following commutation relations [37, Chap. 6]:

$$[\hat{c}_i(\omega), \hat{c}_j^\dagger(t)] = [\hat{d}_i(\omega), \hat{d}_j^\dagger(t)] = \frac{1}{\sqrt{2\pi}} \delta_{ij} e^{-i\omega t}, \quad (\text{A1})$$

which follow from

$$[\hat{c}_i(\omega), \hat{c}_j^\dagger(t)] = \frac{1}{\sqrt{2\pi}} \delta_{ij} \int d\omega' e^{-i\omega' t} [\hat{c}_i(\omega), \hat{c}_j^\dagger(\omega')] = \frac{1}{\sqrt{2\pi}} \delta_{ij} \int d\omega' e^{-i\omega' t} \delta(\omega - \omega') = \frac{1}{\sqrt{2\pi}} \delta_{ij} e^{-i\omega t}.$$

First, we evaluate

$$\begin{aligned} \langle \psi | \hat{c}_1^\dagger(t) \hat{c}_2^\dagger(t + \tau) | 0 \rangle &= \frac{1}{2} \langle 0 | \int d\omega \phi(\omega) e^{-i\omega\delta} \sqrt{\alpha} [-i\hat{c}_1(\omega) + \hat{c}_2(\omega)] [\hat{c}_1(\omega_p - \omega) - i\hat{c}_2(\omega_p - \omega)] \hat{c}_1^\dagger(t) \hat{c}_2^\dagger(t + \tau) | 0 \rangle \\ &= \frac{1}{2\pi} \frac{\sqrt{\alpha}}{2} \int d\omega \phi(\omega) e^{-i\omega\delta} (-e^{-i\omega t} e^{-i(\omega_p - \omega)(t + \tau)} + e^{-i(\omega_p - \omega)t} e^{-i\omega(t + \tau)}) \\ &= \frac{\sqrt{\alpha}}{4\pi} e^{-i\omega_p t} \int d\omega \phi(\omega) e^{-i\omega\delta} (e^{-i\omega\tau} - e^{-i\omega_p\tau} e^{i\omega\tau}). \end{aligned} \quad (\text{A2})$$

Then, multiplying Eq. (A2) by its conjugate we obtain

$$\begin{aligned} \langle \psi | \hat{c}_1^\dagger(t) \hat{c}_2^\dagger(t + \tau) | 0 \rangle \langle 0 | \hat{c}_2(t + \tau) \hat{c}_1(t) | \psi \rangle &= \frac{\alpha}{16\pi^2} \int d\omega_1 \int d\omega_2 \phi(\omega_1) \phi^*(\omega_2) e^{-i(\omega_1 - \omega_2)\delta} \\ &\quad \times (e^{-i\omega_1\tau} - e^{-i\omega_p\tau} e^{i\omega_1\tau}) (e^{i\omega_2\tau} - e^{i\omega_p\tau} e^{-i\omega_2\tau}) \\ &= \frac{\alpha\sigma}{\sqrt{32\pi^3}} e^{-2\sigma^2(\delta + \tau)^2} (e^{4\delta\sigma^2\tau} - 1)^2 \end{aligned} \quad (\text{A3})$$

Next, we evaluate

$$\begin{aligned} \langle \psi | \hat{c}_1^\dagger(t) \hat{d}_2^\dagger(t + \tau) | 0 \rangle &= \frac{1}{2} \langle 0 | \int d\omega \phi(\omega) e^{-i\omega\delta} (\sqrt{\alpha} [-i\hat{c}_1(\omega)] + \sqrt{1 - \alpha} [\hat{d}_2(\omega)]) [\hat{c}_1(\omega_p - \omega)] \hat{c}_1^\dagger(t) \hat{d}_2^\dagger(t + \tau) | 0 \rangle \\ &= \frac{\sqrt{1 - \alpha}}{4\pi} \int d\omega \phi(\omega) e^{-i\omega\delta} e^{-i(\omega_p - \omega)t} e^{-i\omega(t + \tau)} \\ &= \frac{\sqrt{1 - \alpha}}{4\pi} \int d\omega \phi(\omega) e^{-i\omega\delta} e^{-i\omega_p t} e^{-i\omega\tau}. \end{aligned} \quad (\text{A4})$$

Again, multiplying by its conjugate we find

$$\begin{aligned} \langle \psi | \hat{c}_1^\dagger(t) \hat{d}_2^\dagger(t + \tau) | 0 \rangle \langle 0 | \hat{d}_2(t + \tau) \hat{c}_1(t) | \psi \rangle &= \frac{1 - \alpha}{16\pi^2} \int d\omega_1 \int d\omega_2 \phi(\omega_1) \phi^*(\omega_2) e^{-i(\omega_1 - \omega_2)\delta} (e^{-i\omega_1\tau}) (e^{i\omega_2\tau}) \\ &= \frac{(1 - \alpha)\sigma}{\sqrt{32\pi^3}} e^{-2\sigma^2(\delta + \tau)^2}. \end{aligned} \quad (\text{A5})$$

Similarly, we evaluate

$$\begin{aligned}
\langle \psi | \hat{d}_1^\dagger(t) \hat{c}_2^\dagger(t + \tau) | 0 \rangle &= \frac{1}{2} \langle 0 | \int d\omega \phi(\omega) e^{-i\omega\delta} (\sqrt{\alpha}[\hat{c}_2(\omega)] + \sqrt{1-\alpha}[-i\hat{d}_1(\omega)]) [-i\hat{c}_2(\omega_p - \omega)] \hat{d}_1^\dagger(t) \hat{c}_2^\dagger(t + \tau) | 0 \rangle \\
&= -\frac{\sqrt{1-\alpha}}{4\pi} \int d\omega \phi(\omega) e^{-i\omega\delta} e^{-i(\omega_p - \omega)(t+\tau)} e^{-i\omega t} \\
&= -\frac{\sqrt{1-\alpha}}{4\pi} \int d\omega \phi(\omega) e^{-i\omega\delta} e^{-i\omega_p(t+\tau)} e^{i\omega\tau}.
\end{aligned} \tag{A6}$$

And therefore

$$\begin{aligned}
\langle \psi | \hat{d}_1^\dagger(t) \hat{c}_2^\dagger(t + \tau) | 0 \rangle \langle 0 | \hat{c}_2(t + \tau) \hat{d}_1(t) | \psi \rangle &= \frac{1-\alpha}{16\pi^2} \int d\omega_1 \int d\omega_2 \phi(\omega_1) \phi^*(\omega_2) e^{-i(\omega_1 - \omega_2)\delta} (e^{i\omega_1\tau}) (e^{-i\omega_2\tau}) \\
&= \frac{(1-\alpha)\sigma}{\sqrt{32\pi^3}} e^{-2\sigma^2(\delta-\tau)^2}.
\end{aligned} \tag{A7}$$

We can now sum up Eqs. (A3, A5, A7), and normalise to obtain Eq. (10).

2. HOM bunching probability

Deriving the fundamental bunching rate follows similarly. We seek to evaluate $P_b(\tau) = \langle \psi | \hat{\Pi}_b(\tau) | \psi \rangle$, with the bunching POVMs $\hat{\Pi}_b(\tau)$ given in Eq. (9). The key difference is we now look for cases where photons arrive at the same detector.

We start by evaluating

$$\begin{aligned}
\langle \psi | \hat{c}_1^\dagger(t) \hat{c}_1^\dagger(t + \tau) | 0 \rangle &= \frac{1}{2} \langle 0 | \int d\omega \phi(\omega) e^{-i\omega\delta} \sqrt{\alpha}[-i\hat{c}_1(\omega)][\hat{c}_1(\omega_p - \omega)] \hat{c}_1^\dagger(t) \hat{c}_1^\dagger(t + \tau) | 0 \rangle \\
&= -i \frac{\sqrt{\alpha}}{4\pi} \int d\omega \phi(\omega) e^{-i\omega\delta} (e^{-i\omega t} e^{-i(\omega_p - \omega)(t+\tau)} + e^{-i(\omega_p - \omega)t} e^{-i\omega(t+\tau)}) \\
&= -i \frac{\sqrt{\alpha}}{4\pi} e^{-i\omega_p t} \int d\omega \phi(\omega) e^{-i\omega\delta} (e^{-i\omega\tau} + e^{-i\omega_p\tau} e^{i\omega\tau}).
\end{aligned} \tag{A8}$$

Multiplying by its conjugate, we obtain

$$\begin{aligned}
\langle \psi | \hat{c}_1^\dagger(t) \hat{c}_1^\dagger(t + \tau) | 0 \rangle \langle 0 | \hat{c}_1(t + \tau) \hat{c}_1(t) | \psi \rangle &= \frac{\alpha}{16\pi^2} \int d\omega_1 \int d\omega_2 \phi(\omega_1) \phi^*(\omega_2) e^{-i(\omega_1 - \omega_2)\delta} \\
&\quad \times (e^{-i\omega_1\tau} + e^{-i\omega_p\tau} e^{i\omega_1\tau}) (e^{i\omega_2\tau} + e^{i\omega_p\tau} e^{-i\omega_2\tau}) \\
&= \frac{\alpha\sigma}{\sqrt{32\pi^3}} e^{-2\sigma^2(\delta+\tau)^2} (e^{4\delta\sigma^2\tau} + 1)^2
\end{aligned} \tag{A9}$$

For the next two terms, we note that that \hat{c}^\dagger and \hat{d}^\dagger modes are independent. They do not interfere at the beamsplitter, therefore these terms depend only on arrival time and have the same probability as if they arrived at different detectors. Therefore

$$\begin{aligned} \langle \psi | \hat{c}_1^\dagger(t) \hat{d}_1^\dagger(t + \tau) | 0 \rangle \langle 0 | \hat{d}_1(t + \tau) \hat{c}_1(t) | \psi \rangle &= \langle \psi | \hat{c}_1^\dagger(t) \hat{d}_2^\dagger(t + \tau) | 0 \rangle \langle 0 | \hat{d}_2(t + \tau) \hat{c}_1(t) | \psi \rangle \\ &= \frac{(1 - \alpha)\sigma}{\sqrt{32\pi^3}} e^{-2\sigma^2(\delta + \tau)^2} \end{aligned} \quad (\text{A10})$$

and

$$\begin{aligned} \langle \psi | \hat{d}_1^\dagger(t) \hat{c}_1^\dagger(t + \tau) | 0 \rangle \langle 0 | \hat{c}_1(t + \tau) \hat{d}_1(t) | \psi \rangle &= \langle \psi | \hat{d}_1^\dagger(t) \hat{c}_2^\dagger(t + \tau) | 0 \rangle \langle 0 | \hat{c}_2(t + \tau) \hat{d}_1(t) | \psi \rangle \\ &= \frac{(1 - \alpha)\sigma}{\sqrt{32\pi^3}} e^{-2\sigma^2(\delta - \tau)^2}. \end{aligned} \quad (\text{A11})$$

As before, we sum up Eqs. (A9, A10, A11), and normalise to obtain Eq. (11).

3. No-HOM arrival probability

For our no-HOM protocol, we are concerned only with arrival times. We recall our POVMs $\hat{\Pi}^{\text{NH}}(\tau)$, as given in Eq. (31), and want to fully derive $P^{\text{NH}}(\tau) = \langle \psi | \hat{\Pi}^{\text{NH}}(\tau) | \psi \rangle$. As we no longer have a beamsplitter present, the photons never interact after being generated and there is no dependence on their relative indistinguishability, and detectors cannot distinguish between the \hat{a}^\dagger and \hat{b}^\dagger modes so we are free to treat these as equivalent. We can thus set $\alpha = 1$ for simplicity and work with the state in the form

$$|\psi\rangle = \int d\omega \phi(\omega) e^{i\omega\delta} \hat{a}_i^\dagger(\omega) \hat{a}_s^\dagger(\omega_p - \omega) |0\rangle \quad (\text{A12})$$

and likewise use the simplified POVMs

$$\hat{\Pi}^{\text{NH}}(\tau) = \hat{a}_i^\dagger(t) \hat{a}_s^\dagger(t + \tau) |0\rangle \langle 0| \hat{a}_s(t + \tau) \hat{a}_i(t). \quad (\text{A13})$$

We first evaluate

$$\begin{aligned} \langle \psi | \hat{a}_i^\dagger(t) \hat{a}_s^\dagger(t + \tau) | 0 \rangle &= \langle 0 | \int d\omega \phi(\omega) e^{-i\omega\delta} \hat{a}_i^\dagger(\omega) \hat{a}_s^\dagger(\omega_p - \omega) \hat{a}_i^\dagger(t) \hat{a}_s^\dagger(t + \tau) | 0 \rangle \\ &= \int d\omega \phi(\omega) e^{-i\omega\delta} e^{-i(\omega_p - \omega)(t + \tau)} e^{-i\omega t} \\ &= \int d\omega \phi(\omega) e^{-i\omega\delta} e^{-i\omega_p(t + \tau)} e^{i\omega\tau}. \end{aligned} \quad (\text{A14})$$

Multiplying by its conjugate we then obtain

$$\begin{aligned} \langle \psi | \hat{a}_i^\dagger(t) \hat{a}_s^\dagger(t + \tau) | 0 \rangle \langle 0 | \hat{a}_s(t + \tau) \hat{a}_i(t) | \psi \rangle &= \int d\omega_1 \int d\omega_2 \phi(\omega_1) \phi^*(\omega_2) e^{-i(\omega_1 - \omega_2)\delta} (e^{i\omega_1\tau}) (e^{-i\omega_2\tau}) \\ &= 2\sqrt{2\pi}\sigma e^{-2\sigma^2(\delta - \tau)^2}, \end{aligned} \quad (\text{A15})$$

which normalises to Eq. (32).

Appendix B: Fundamental limits

For the QFI calculation we must evaluate the quantities $\langle \partial_\delta \psi | \psi \rangle$ and $\langle \partial_\delta \psi | \partial_\delta \psi \rangle$. We first evaluate the overlap $\langle \partial_\delta \psi | \psi \rangle$:

$$\begin{aligned}
\langle \partial_\delta \psi | \psi \rangle &= \frac{1}{V} \int d\omega_1 \int d\omega_2 \phi(\omega_1) \phi(\omega_2) (-i\omega_1) e^{-i\omega_1 \delta} e^{i\omega_2 \delta} \\
&\quad \times (\alpha \langle 0 | \hat{a}_s(\omega_p - \omega_1) \hat{a}_i(\omega_1) \hat{a}_i^\dagger(\omega_2) \hat{a}_s^\dagger(\omega_p - \omega_2) | 0 \rangle \\
&\quad + (1 - \alpha) \langle 0 | \hat{a}_s(\omega_p - \omega_1) \hat{b}_i(\omega_1) \hat{b}_i^\dagger(\omega_2) \hat{a}_s^\dagger(\omega_p - \omega_2) | 0 \rangle) \\
&= -\frac{i}{V} \int d\omega_1 \int d\omega_2 \phi(\omega_1) \phi(\omega_2) \omega_1 e^{-i\omega_1 \delta} e^{i\omega_2 \delta} \delta_D((\omega_p - \omega_2) - (\omega_p - \omega_1)) \delta_D(\omega_2 - \omega_1) \\
&= -\frac{i}{V} \int d\omega \phi(\omega)^2 (\omega_p - \omega) \delta_D(0) \\
&= -\frac{i\omega_p}{2}.
\end{aligned} \tag{B1}$$

We can similarly evaluate the overlap $\langle \partial_\delta \psi | \partial_\delta \psi \rangle$ to find

$$\begin{aligned}
\langle \partial_\delta \psi | \partial_\delta \psi \rangle &= \frac{1}{V} \int d\omega \phi(\omega)^2 \omega^2 \delta_D(0) \\
&= \sigma^2 + \frac{\omega_p^2}{4}.
\end{aligned} \tag{B2}$$

We then combine these with Eq. (26) to obtain the QFI as given in Eq. (30).

Appendix C: Fisher information matrices without time-resolution

Without time-resolution we have a finite number of measurement outcomes. It is therefore simple to show the full form of the FIM, for both detector types.

1. Bucket detectors

Let $\boldsymbol{\theta} = (\delta, \alpha, \sigma, \gamma)$ be the vector of potentially unknown parameters. Then for bucket detectors without time-resolution, with elements as defined in Eq. (24), our FIM takes the form

$$\mathbf{F}^B(\boldsymbol{\theta}) = \begin{pmatrix} 16\alpha^2\delta^2\kappa\sigma^4 & -4\alpha\delta\kappa\sigma^2 & 16\alpha^2\delta^3\kappa\sigma^3 & 8\alpha\delta\sigma^2\chi \\ -4\alpha\delta\kappa\sigma^2 & \kappa & -4\alpha\delta^2\kappa\sigma & -2\chi \\ 16\alpha^2\delta^3\kappa\sigma^3 & -4\alpha\delta^2\kappa\sigma & 16\alpha^2\delta^4\kappa\sigma^2 & 8\alpha\delta^2\sigma\chi \\ 8\alpha\delta\sigma^2\chi & -2\chi & 8\alpha\delta^2\sigma\chi & -\frac{8\chi e^{2\delta^2\sigma^2}}{(1-\gamma)^2} \end{pmatrix}, \tag{C1}$$

with

$$\begin{aligned}
\kappa &= \frac{(1-\gamma)^2(1+\gamma)}{\alpha^2(\gamma-1) - 4\alpha\gamma e^{2\delta^2\sigma^2} + (3\gamma+1)e^{4\delta^2\sigma^2}}, \\
\chi &= \frac{1-\gamma}{\alpha(\gamma-1) - (3\gamma+1)e^{2\delta^2\sigma^2}}.
\end{aligned} \tag{C2}$$

This matrix is rank 2, therefore it is singular and a multiparameter estimation of all four parameters is impossible. Only submatrices covering exactly one of $\{\delta, \alpha, \sigma\}$ along with γ are non-singular. It is therefore possible to

estimate the photon loss at the same time as estimating any one of the other parameters. The singularity of this matrix is removed through the introduction of time-resolution.

2. Number-resolving detectors

For number-resolving detectors without time-resolution, our FIM now takes the form

$$\mathbf{F}^{\text{NR}}(\boldsymbol{\theta}) = \begin{pmatrix} 16\alpha^2\delta^2\xi\sigma^4 & -4\alpha\delta\xi\sigma^2 & 16\alpha^2\delta^3\xi\sigma^3 & 0 \\ -4\alpha\delta\xi\sigma^2 & \xi & -4\alpha\delta^2\xi\sigma & 0 \\ 16\alpha^2\delta^3\xi\sigma^3 & -4\alpha\delta^2\xi\sigma & 16\alpha^2\delta^4\xi\sigma^2 & 0 \\ 0 & 0 & 0 & \frac{2}{\gamma-\gamma^2} \end{pmatrix}, \tag{C3}$$

with

$$\xi = \frac{(1-\gamma)^2}{e^{4\delta^2\sigma^2} - \alpha^2}. \tag{C4}$$

Once again, this matrix is rank 2. The key difference here is that by eliminating the bunching/loss ambiguity γ is now wholly independent, this manifests in the FIM by setting all off-diagonal terms involving γ to zero. This means that γ can be estimated even if none of the other parameters are known, the estimation will be just as efficient regardless of what the other parameters are set to, and estimating γ simultaneously with any other parameters will not harm the efficiency of the other estimations. As before the singularity vanishes once time-resolution is introduced, though there is still some correlation between δ , α , and σ .

3. Perfect visibility

From Eqs. (C1) and (C2), we see for bucket HOM the single-parameter CFI $F_\delta^B = [\mathbf{F}^B(\boldsymbol{\theta})]_{1,1}$ takes the form

$$F_\delta^B = \frac{16\alpha^2(1-\gamma)^2(\gamma+1)\delta^2\sigma^4}{\alpha^2(\gamma-1) - 4\alpha\gamma e^{2\delta^2\sigma^2} + (3\gamma+1)e^{4\delta^2\sigma^2}}. \quad (\text{C5})$$

As we approach perfect visibility, $\alpha \rightarrow 1$, and in the limit $\delta \rightarrow 0$, we obtain $F_\delta^B \rightarrow 4\sigma^2(1-\gamma)^2 = H_\delta(\gamma)$, the QFI conditioned on γ . Similarly from Eqs. (C3) and (C4) the NR HOM single-parameter CFI $F_\delta^{\text{NR}} = [\mathbf{F}^{\text{NR}}(\boldsymbol{\theta})]_{1,1}$ takes the form

$$F_\delta^{\text{NR}} = \frac{16\alpha^2(1-\gamma)^2\delta^2\sigma^4}{e^{4\delta^2\sigma^2} - \alpha^2}. \quad (\text{C6})$$

Like with bucket detectors, by letting $\alpha \rightarrow 1$ and $\delta \rightarrow 0$, we find $F_\delta^{\text{NR}} \rightarrow 4\sigma^2(1-\gamma)^2 = H_\delta^{\text{2ph}}(\gamma)$, and have again recovered the QFI. The maximal information as a function of α is plotted in Fig. 8.

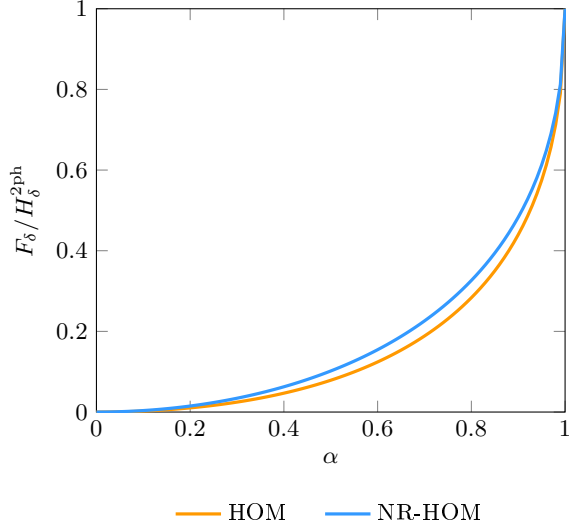


FIG. 8. The relative information $F_\delta / H_\delta^{\text{2ph}}$ for our non-time-resolving protocols. We set $\gamma = 0.4$, choose δ to maximise information, and vary α . As we approach $\alpha = 1$, the two information peaks converge, leading to a single peak at $\delta = 0$ where $F_\delta = H_\delta^{\text{2ph}}$ and we have reached the QFI limit.

Appendix D: Estimating other parameters

We have throughout this paper focused on estimation of the delay δ . A key merit of our time-resolving HOM protocols is that they allow δ to be estimated even when other parameters are unknown, streamlining the calibration process compared to previous protocols. We now briefly examine the CFI for these other parameters and discuss how they might best be estimated.

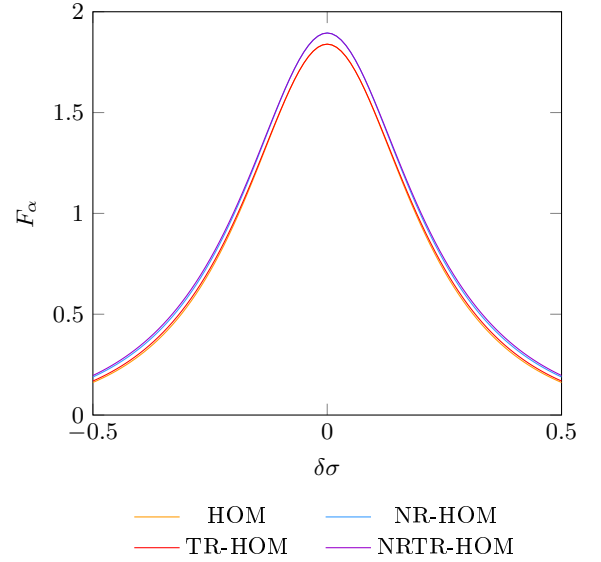


FIG. 9. Comparison of the CFI F_σ for our various protocol configurations, as we vary the delay δ . We set $\alpha = 0.9$, $\gamma = 0.4$, $T = 5/\sigma$. The information peaks at $\delta = 0$, where coincidence and bunching rates vary most rapidly with α . The benefits of time-resolution are small, both bucket curves closely overlap, as do both number-resolving curves, and at $\delta = 0$ the difference in information between time-resolving and non-time-resolving protocols vanishes.

We discussed in Sec. VI how estimating both δ and α simultaneously shifted the optimal estimation points closer to the origin compared to those when just estimating δ . We can here see, in Fig. 9, that the CFI F_σ indeed peaks exactly at the origin, this being the optimal place to estimate α alone as here the coincidence and bunching rates are most sensitive to changes in the visibility.

We see in Fig. 10 how the CFI F_σ varies with δ . When all other parameters are known, the optimum position to estimate σ is with δ at either of the peaks. Suppose that we want to estimate σ simultaneously with both δ and α . The peaks in F_σ lie further from the origin compared to the peaks for F_δ . While estimating α with δ pulls the optimum estimation points inward, the additional requirement of estimating σ will again pull them back outwards.

For γ , we previously noted in Appendix C that when number-resolving detectors are used this becomes an independent parameter, and can be estimated trivially without impacting the estimation of any other parameters. When using bucket detectors, we treated γ as a calibration parameter, obtained very simply by tuning ourselves far outside the dip. Even though γ is not independent in this case, it can still be estimated simultaneously with other parameters. F_γ is also independent of any time-resolution for our detectors.

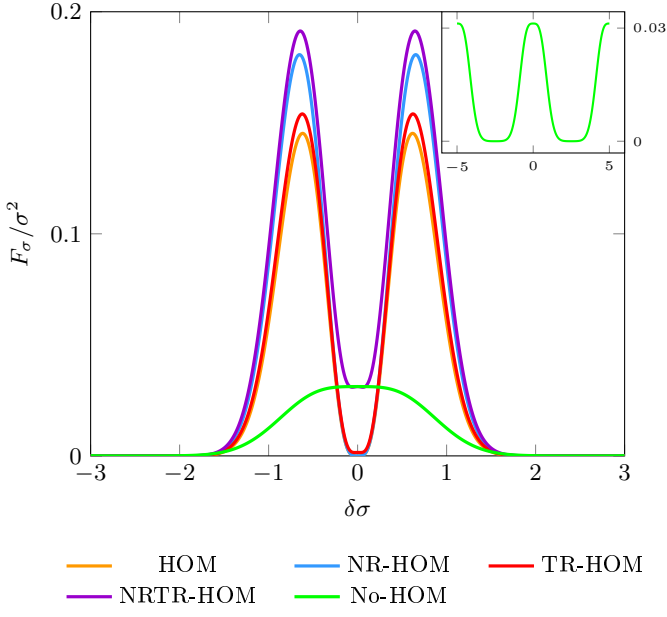


FIG. 10. Comparison of the CFI F_σ for our various protocol configurations, as we vary the delay δ . We set $\alpha = 0.9$, $\gamma = 0.4$, $T = 5/\sigma$. These follow a similar shape to the plots of F_δ in Fig. 3; the main differences being that the peaks are narrower, more spread out, and for TR-HOM and NRTR-HOM F_σ does not dip all the way to zero at the origin. With the inset we can see that the no-HOM information follows a similar oscillatory pattern, with maxima and minima in the same positions but an overall more squared curve.

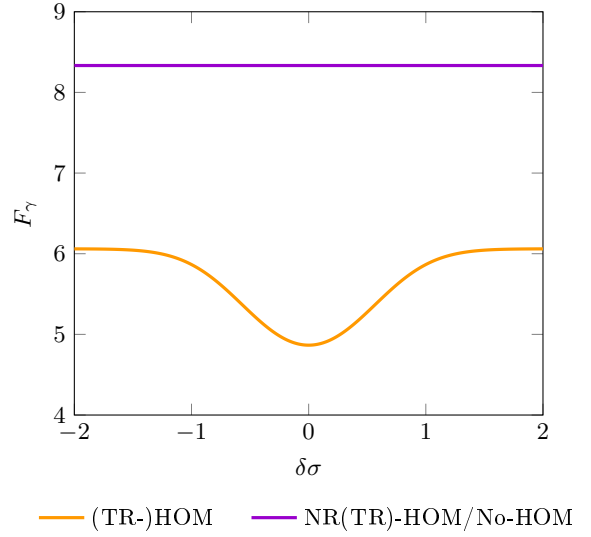


FIG. 11. Comparison of the CFI F_γ for our various protocol configurations, as we vary the delay δ . We set $\alpha = 0.9$ and $\gamma = 0.4$. No-HOM is functionally identical to NR(TR)-HOM in regards to F_γ , as the photons are always directed to separate detectors. In these cases the information is constant. For (TR)-HOM, the information is reduced somewhat due to the bunching/loss ambiguity. It tends to a constant for large δ , but further dips slightly near the origin where bunching is more likely.

In Fig. 11 we see a constant F_γ when number-resolving detectors are used. This is also the case for our no-HOM protocol, as each photon always arrives at a different detector. Bucket detectors perform slightly worse, and we see an additional small dip near the origin. There is no dependence on time-resolution. Therefore, when using bucket detectors for our HOM protocol, a requirement to estimate γ with the other parameters would further push the optimal estimation point outwards once again.